

Unraveling the Energetic Landscape of Perovskite Solar Cells: A Synergy of 2D Drift-Diffusion Simulations and Tapered Cross-Section Photoelectron Spectroscopy

Clemens Baretzky, Clément Maheu, Markus Frericks, Thomas Mayer, and Uli Würfel*

Interfaces are crucial elements that define the electronic properties of perovskite solar cells (PSCs). However, obtaining the band structure of a full PSC and accessing its buried layers and interfaces without modifying the device is challenging. A tapered cross section (TCS) of a PSC (i.e., a PSC polished under a very shallow angle) offers access to these buried parts on a width one or two orders of magnitude larger than the lateral resolution of a photoelectron spectroscopy (PES) set-up. Herein, 2D numerical drift-diffusion simulations are combined with TCS-PES measurements to access the electrostatic potential profile with high spatial resolution along the PSC, allowing us to construct the band diagram of device. Thus, it is confirmed experimentally that the presence of a band bending at the interfaces between perovskite and charge-transport layers and quantified under various conditions relevant to solar cell operation. Such synergy between the TCS-PES approach and numerical simulation provides substantial information about the energetic landscape at the interfaces in PSCs and is essential for devices without mostly field-free layers. These insights for dark and illuminated conditions are central to understand the nature of interfaces within PSCs.

as well as a better understanding of the materials.^[2] Interfaces have been found to be the main reason for the efficiency limits and thus require extensive characterization to further improve performance.^[3] The only technique for investigating interfaces that provide electronic and spectroscopic (i.e., chemical) information at the same time is photoelectron spectroscopy (PES), which has already been used extensively to characterize PSCs.^[4,5] Indeed, binding energies measured by PES are not only characteristic of a given element or an oxidation state but also they can be used to extract electrostatic potential (cf. Section S2.1, Equation (S2.8), Supporting Information). The energy difference between the Fermi level of a material and its core levels or valence band states can be measured by PES at different positions of the interface of a junction and assigned to band bending. However, performing PES on these interfaces requires

1. Introduction


The tremendous progress of perovskite solar cells (PSCs) has led to certified efficiencies reaching 25.7%.^[1] It has been achieved due to continuous optimization of the manufacturing techniques

accessing them without modifying the characteristics of the device.^[6] Accessing the interfaces by preparation and investigation of a normal cross section is not feasible due to low lateral resolution of standard PES set-up (i.e., above 10 μm and up to several hundreds of micrometers) compared with the thickness of typical perovskite solar cells and especially with the extensions of the space charge regions within. Approaches to overcome this limitation exist and can be classified as bottom-up or top-down approaches.^[2,7]

C. Baretzky, U. Würfel
Fraunhofer Institute for Solar Energy Systems ISE
Heidenhofstraße 2, 79110 Freiburg, Germany
E-mail: uli.wuerfel@ise.fraunhofer.de

C. Baretzky, U. Würfel
Freiburg Materials Research Center FMF
University of Freiburg
Stefan-Meier-Straße 21, 79104 Freiburg, Germany

C. Maheu, M. Frericks, T. Mayer
Surface Science Laboratory
Department of Materials and Earth Sciences
Technical University of Darmstadt
Otto-Berndt-Strasse 3, 64287 Darmstadt, Germany

 The ORCID identification number(s) for the author(s) of this article can be found under <https://doi.org/10.1002/solr.202300355>.

© 2023 The Authors. Solar RRL published by Wiley-VCH GmbH. This is an open access article under the terms of the Creative Commons Attribution License, which permits use, distribution and reproduction in any medium, provided the original work is properly cited.

DOI: 10.1002/solr.202300355

For the bottom-up approach, the main method is the so-called step-by-step interface experiment that consists of alternating between PES measurements and the stepwise deposition of thin layers of material on top of a substrate.^[8] It has been used for investigating the interface energetics of perovskite absorbers with hole transport layers (HTL) or electron transport layers (ETL), e.g., poly[bis(4-phenyl)(2,4,6-trimethylphenyl)amine (PTAA), 1,4,5,8,9,11-Hexaazatriphenylenehexacarbonitrile (HATCN), copper(II) phthalocyanine (CuPc), C₆₀, rubrene, CuI, or 2,2',7,7'-Tetrakis[N,N-di(4-methoxyphenyl)amino]-9,9'-spirobi-fluorene (Spiro-OMeTAD)].^[9–16] The step-by-step interface experiment requires a cluster tool in which samples can be transferred under a controlled atmosphere between vacuum deposition chambers and the PES analysis chamber.

In contrast, the main asset of the top-down approaches is characterizing the chemical and the electronic properties of externally

prepared full devices increasing the information depth using hard X-Ray PES, using depth profiling PES, or our recently introduced tapered cross-section PES (TCS-PES).^[17–21] Depth profiling PES investigates a device by alternating PES measurements and sputtering with single ion or cluster ion sources to stepwise remove the different layers. However, this process can induce damage, e.g., Pb⁰ generation, if the ions are not chosen carefully; the use of large molecules such as Ar-clusters or coronene minimizes the material's damage.^[17–20]

This work is focused on coupling the experimental TCS-PES approach, as depicted in **Figure 1** with numerical simulations (**Figure 2**) to retrieve a consistent energetic landscape of the full

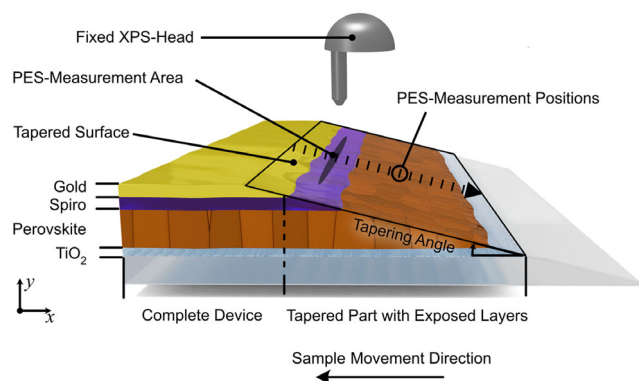


Figure 1. Overview of the tapered cross-section PES approach. A segment of a complete, planar PSC is ground to a tapered structure. This exposes the intermediate layers at the tapered surface. Due to the shallow tapering angle, this allows to investigate separate layers and their interfaces with UPS and XPS by moving the sample relative to the PES-Detector.

device. The experiment consists in creating a cross-section with an extremely small angle, the so-called tapered cross-section. It converts a normal cross-section of a few hundred nanometers into a tapered cross-section with a width of millimeters. The different layers are then exposed on the tapered cross-section surface, and they are larger than the usual lateral resolution of the PES set-up (i.e., more than 10 μm) so chemical and electronic properties of each individual layer and their interfaces can be measured by moving the sample horizontally under the detector (Figure 1). So far, TCS has been prepared with a metallographic polishing machine, a drilling machine or ultra-low-angle microtomy.^[6,20,21,22,23–25] The essential condition for utilizing the binding energy variation at the interfaces on the TCS to infer the band diagram of the entire device is, that the TCS preparation process should not alter it. Surface states created on the TCS may induce band bending toward the TCS as artifacts and disturb the band bending along the device. This was the case for III-V semiconductor devices (e.g., GaInP on Ge and GaAs substrates) that were strongly disturbed by Fermi-level pinning to the surface states created by the polishing procedure, also rendering it impossible to measure binding energy shifts due to illumination.^[6] In contrast, perovskites with their shallow gap states are unaffected by this phenomenon and previous works have shown that it is possible to extract reliable information on the electronic properties of PSCs.^[25] Moreover, the binding energies observed in TCS layers, along with their change under illumination, are in good agreement with previous measurements from half-cells that were not subjected to the TCS-preparation method.^[15]

TCS-PES measurements were conducted on the following cell stack Au/Spiro-OMeTAD/(FAPbI₃)_{0.85}(MAPbBr₃)_{0.15}/m-TiO₂/c-TiO₂/FTO. The measured binding energy variations under dark

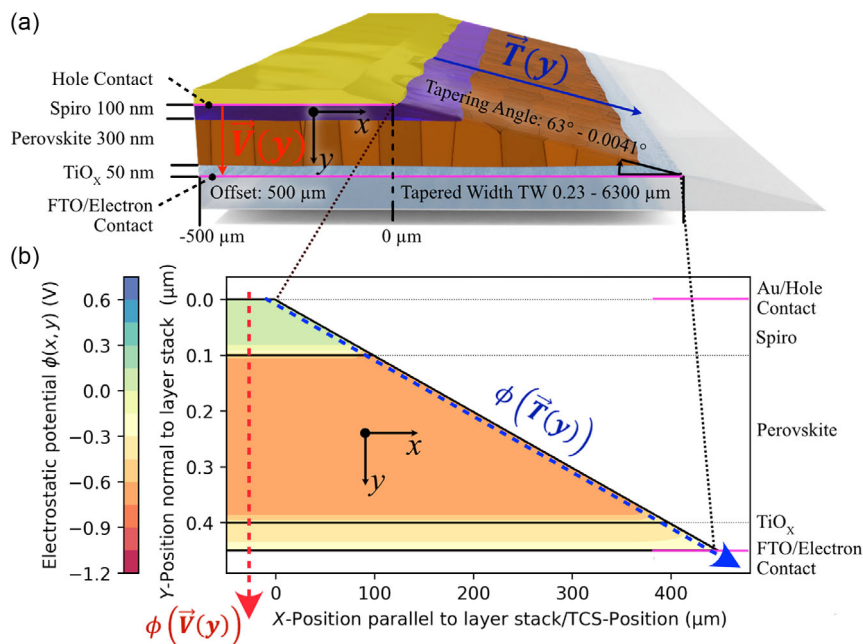


Figure 2. a) Scheme of the tapered cross-section geometry used in the simulation. b) Map of the simulated electrostatic potential of the tapered device. On the x -axis, below 0 μm refers to the *full device*. On the x -axis, the 0 to 440 μm refers to the *tapered part* of the device (i.e., tapered width of 440 μm). The vertical electrostatic potential between the contacts is denoted as $\phi(\vec{V})$ and the one along the taper as $\phi(\vec{T})$. Note that there is an aspect ratio of almost 1:1000 between the y -axis and the x -axis as depicted more accurately in Figure S1 (Supporting Information).

conditions evidenced a downward band bending of 0.75 eV at the Spiro-OMeTAD|perovskite interface and a slight upward band bending at the perovskite|mesoporous TiO₂ (m-TiO₂) interface under dark conditions. Under illumination (≈ 0.1 sun), almost a light upward band bending was measured. Thus, a photovoltage of 0.81 V was deduced from these XPS and UPS measurements for the given illumination conditions. However, this study does not include remeasuring in the reverse direction, which could help to assess possible changes due to the measurement procedure, i.e., due to X-Ray or charge-up effects.

It is interesting to note that a similar conclusion is stated in another study.^[20] The TCS-PES approach has been performed in a different laboratory on a different device (Ag/Spiro-OMeTAD/Cs_{0.05}(FA_{0.83}MA_{0.17})_{0.95}Pb(I_{0.83}Br_{0.17})₃/m-TiO₂/c-TiO₂/FTO), with a different preparation method for the TCS. A 0.7 eV downward band bending at the Spiro-OMeTAD|perovskite interface was also found.

Considering that across the TCS, the PSC is no longer a complete solar cell, the band bending measured on the tapered part deviates from the band bending at the buried interfaces of the actual planar device. To address this issue, we performed 2D drift-diffusion simulations with Sentaurus TCAD for a tapered device using material parameters from the literature.^[26] These results were compared with the experimental electrostatic potential obtained by TCS-PES and other standard approaches, such as the interface experiment. Then, as a second step, we used the same parameters to systematically investigate deviations of the electrical potential between the tapered part and the planar part, i.e., between both electrodes (Figure 1).

Our findings provide a comprehensive picture of the electrostatic potential at the interfaces within a PSC, highlighting the spatial and temporal changes in energy bands in the dark and under illumination. We can understand why the main band bending seems to appear within the Spiro-OMeTAD layer. Furthermore, we find that the band structure at the perovskite|TiO₂ interface might reduce the extraction efficiency for electrons, pointing to an unrealized potential for the increase of device efficiency by improving the energy band alignment between the perovskite and the TiO₂ layer.

2. Simulation of the Tapered Cross-Section Measurement

For our numerical simulation, we used the following layer thicknesses, based on our previous work as well as literature: 100 nm for the Spiro-OMeTAD layer, 300 nm for the perovskite layer, and 50 nm for the TiO₂ layer, as sketched in Figure 1.^[21,25] Given the high charge carrier densities in FTO and Au, these layers are defined as a metal-type boundary condition along the respective device interfaces. The mesoporous TiO₂ was simplified to a planar layer and merged with the compact TiO₂, because it is a thin layer with high relative permittivity, and the wear of mesoporous TiO₂ interlaced with perovskite during polishing is unknown. To mimic the experimental device geometry, we used a very high aspect ratio (tapered width:device thickness of 1000:1) for the tapered part of the device (i.e., tapered width \gg device thickness), which is more accurately depicted in Figure S1 (Supporting Information). The planar part of the

device to the left of the tapered part has a width of 500 μ m. Finding parameters to realistically simulate a thin film solar cell is challenging due to the many different materials involved. Values for the electron affinities of the conduction band and for the bandgaps were taken from literature for the respective materials.^[27,28] For PSCs, extensive literature exists regarding charge carrier mobilities, effective densities of states, relative permittivities, and other parameters.^[29–32] For the sake of simplicity, equal mobilities for electrons and holes are assumed. Furthermore, mobile ions are disregarded in our analysis. When taking into consideration the given material parameters, Spiro-OMeTAD behaves akin to a p-type layer, whereas both perovskite and TiO₂ demonstrate the properties of n-type material. Importantly, this analysis does not consider Fermi-level pinning or surface charges at the TCS interface. The external boundaries of the device, which are not contacted, adhere to an ideal Neumann boundary condition, while the contacts adhere to a Dirichlet boundary condition.

To simulate the illumination, a homogenous and exponential generation profile, with the same average generation rate have been compared. Both cases gave similar results, mainly due to the high charge carrier mobilities in the perovskite. For the sake of simplicity, only the homogenous illumination profile is used in this work.

Experimentally, it is very difficult to achieve a well-defined illumination environment for dark and illuminated conditions inside an ultra-high vacuum (UHV) machine. Indeed, Hellmann et al. address the issue of residual light inducing binding energy shifts and originating from, for instance, the hot-filament ionization gauge or the visible light of the X-Ray source.^[15] Therefore, the average generation rate within the device is the only free parameter that was varied in the simulations to adjust the simulated data to the experimental one.

The importance of seemingly small illumination intensities can be demonstrated by considering the equation for the quasi-Fermi level splitting (ΔE_F) inside an n-doped absorber under illumination

$$\Delta E_F = k_B T \ln \left(\frac{(n_{e,0} + \Delta n_e)(n_{h,0} + \Delta n_h)}{n_{e,0}n_{h,0}} \right) \quad (1)$$

Here, $n_{e,0}$ and $n_{h,0}$ denote the equilibrium electron and hole charge carrier density, respectively, with the additional charge carrier density Δn_e and Δn_h due to illumination. When the photogenerated charge carriers are few compared to the doping concentration, it follows that $\Delta n_e \ll n_{e,0}$ and $\Delta n_h \gg n_{h,0}$. The general equation of the quasi-Fermi level splitting (1) can be simplified to

$$\Delta E_F = k_B T \ln \left(\frac{\Delta n_h}{n_{h,0}} \right) \quad (2)$$

Under open circuit conditions in the “low-level injection regime”, the steady-state recombination rate R can be described by

$$R = k_{\text{rad}} \Delta n_h n_{e,0} + \frac{\Delta n_h}{\tau_{\text{SRH},h}} \quad (3)$$

with the Shockley–Read–Hall (SRH) recombination lifetime of holes τ_{SRH} . Making the additional assumption that SRH

recombination is the dominating recombination mechanism, the steady-state recombination Equation (3) can be approximated to

$$R = \frac{\Delta n_h}{\tau_{SRH,h}} \quad (4)$$

Under open-circuit conditions, the recombination rate R is equal to the generation rate G and we obtain

$$\Delta E_F = k_B T \ln \left(\frac{G \tau_{SRH}}{n_{h,0}} \right) \quad (5)$$

which shows that ΔE_F depends logarithmically on G . In addition, the reduction in band bending is determined by ΔE_F which in a zero-dimensional approximation is equivalent to V_{OC} . Thus, low residual illumination has a significant impact on the V_{OC} and must be considered when comparing simulations to the experimental results. In complete solar cells, low residual illumination does not necessarily lead to a significant quasi-Fermi level splitting ΔE_F inside the absorber if the parallel resistance R_p is so low that it effectively shunts the device. Here, this is not the case for two reasons. PSCs have been shown to reach very high R_p values which make them suitable for low-light applications.^[33] In addition, a tapered device with localized shunts (i.e., pinhole defects) is insulated due to the missing top contact, R_p is therefore expected to be orders of magnitude larger than a standard solar cell.

To compare the simulation results with measurements, and the expected electrostatic potential in a planar device, 1D cross-sectional electrostatic potentials were extracted along two lines. One vertical line between the contacts with $\phi(\vec{V})$ 500 μm away from the tapered interface, and one line along the tapered surface as measured with the TCS-PES approach $\phi(\vec{T})$. This scheme is illustrated in Figure 2.

3. Experimental Section

3.1. Tapered Cross-Section Measurements

In our previous work, we measured along the TCS, the XPS spectra of eight core levels (Au4f_{7/2}, C1s, N1s, Pb4f_{7/2}, I3d_{5/2}, Br3d_{5/2}, Ti2p_{3/2}, Sn3d_{5/2}).^[25] From the intensity variation, we identified the area of the TCS corresponding to the six layers of the device: Au top electrode (Au4f_{7/2}), Spiro-OMeTAD as the HTL (C1s), perovskite absorber ((FAPbI₃)_{0.85}(MAPbBr₃)_{0.15}) (C1s, N1s, Pb4f_{7/2}, I3d_{5/2}), the m-TiO₂/perovskite (Ti2p_{3/2} in addition) and the compact TiO₂ as the ETL (only Ti2p_{3/2}), and the fluorine-doped SnO₂ (FTO) substrate (Sn3d_{5/2}). Five of these eight core levels were then used as characteristic emissions of the PSC layers. We compared the XPS spectra of Au4f_{7/2}; C1s, Pb4f_{7/2}, Ti2p_{3/2}, and Sn3d_{5/2} under dark and light. The top contact of gold was grounded and therefore its Fermi level was in equilibrium with one of the instruments at a binding energy (BE) of 0 eV, while the FTO contact was floating. All core and valence band levels are then discussed relative to this reference Fermi level. Further experimental details are given in Section S1 (Supporting Information). For each illumination condition, the measurement was performed only one time and in the direction from the Au contact to the bottom FTO contact.

The binding energy position of Au4f_{7/2}, C1s, Pb4f_{7/2}, Sn3d_{5/2}, and Ti2p_{3/2} orbitals was recorded in the dark, and under illumination on the tapered cross-section. The experimental electrostatic potential was defined as the difference in binding energy relative to a reference level, as exemplified in Figure S3 (Supporting Information). This reference is chosen as an intrinsic characteristic of the layer (e.g., 84.0 eV for the Au4f_{7/2} emission line of gold or 284.4 eV for the C1s emission line of Spiro-OMeTAD).

A binding energy shift, when observed, can be attributed to either a change in chemical composition or a variation in the electrostatic potential. If the cause is a change in electrostatic potential, the energy difference between the valence band maximum and the core level will remain constant for a specific material composition. Thus, any BE shifts of core levels correspond to parallel shifts of both the valence band maximum and the conduction band minimum. When there is a BE shift toward lower binding energy, it signifies upward band bending. Conversely, a BE shift toward higher energy indicates downward band bending. By assembling these gradual BE shifts, one can estimate the electrostatic potential across an entire semiconductor device stack. The interplay between band bending, material parameters, and illumination is an intricate aspect rooted in semiconductor physics. In Section S2 (Supporting Information), this is revisited, specifically how material parameters such as the type of semiconductor (n- or p-type), the presence of excess carriers due to illumination, and their interactions can influence band bending at junctions.

The advantage of combining the tapered cross-section photoemission spectroscopy (TCS-PES) approach with drift-diffusion simulations lies in the fact that the simulated electrostatic potential remains unaffected by potential interfacial reactions. Consequently, 2D drift-diffusion simulation serves as a powerful tool to distinguish between changes in electrostatic potential and alterations in chemical composition e.g., by variations of the composition due to ion migration and demixing of the halogens or by compositional variations, e.g., in the m-TiO₂-perovskite layer due to lateral pore size variations.^[25]

The same PES measurement was repeated under illumination. For a functioning and stable perovskite solar cell, we assume that the photogeneration of charge carriers can alter the electrostatic potential but not the chemical composition. While TCS should also be considered a destructive method, the possibility to directly compare subsequent measurements in the dark and under illumination is a key advantage of the TCS-PES as it always provides access to all the different layers and their interfaces. On the contrary, the Ar⁺/cluster depth profiling approach etches layer after layer and needs to remove one interface to study another one.

To mitigate the degradation associated with exposure to photons within the AM1.5G spectrum, the duration of the experiment must be kept below the typical degradation timescales of perovskite solar cells with a given stoichiometry.^[34] Degradation due to exposure to X-Ray photons during PES measurements has been previously reported.^[35] However, the TCS measurement approach inherently mitigates this issue by probing different positions on the sample, thereby, minimizing exposure at each individual location. The grinding process used in TCS-PES measurements can potentially introduce a degree of “roughness” to

the analyzed device. However, given the broad detection area of the PES method, such irregularities are effectively smoothed out in the measurements. This results in data that represent an average behavior across the detection area, thereby minimizing the impact of localized surface variations due to the grinding process.

Thus, we anticipate that the data obtained with our approach will provide a sufficiently accurate representation of the electronic structure, enabling a meaningful discussion concerning the device band structure.

3.2. Comparison of Measurements and Simulations

As depicted in **Figure 3a**, in the dark, at the HTL|perovskite interface, a BE shift of -0.75 V of the C1s Spiro-OMeTAD emission (centered at 284.6 eV, purple downward triangles), and no BE shift of the perovskite Pb4f_{7/2} core level (brown downward triangle) have been observed. If this shift is not due to chemical composition variation, it indicates a downward band bending at the HTL|perovskite, and more precisely inside the Spiro-OMeTAD (See Figure 3a). Under light, the overall BE shift corresponds to $+0.06$ eV. The sum of the BE-shifts between dark and light is therefore around 0.81 eV.

This band bending at the HTL|perovskite interface is reproducible. Indeed, with a completely different device measured

by TCS-PES, Das et al. observed a similar band bending (See Figure S3, Supporting Information) in which the overall BE shifts were extracted and plotted along the tapered cross-section).

Also, at the perovskite|ETL interface, BE shifts of the Pb4f_{7/2} and the Ti2p_{3/2} core levels are observed. Under dark conditions, the Ti2p_{3/2} emission is shifted by $+0.2$ eV, and the Pb4f_{7/2} emission is shifted by -0.4 eV. As similar values were also observed under illumination, in our previous work we therefore hypothesized that these shifts were due to chemical composition variation and not electronic ones.^[25] However here, the 2D drift-diffusion simulations, that does not consider chemical composition variation, also show that a 0.5 eV upward band bending exists at the perovskite|ETL interface. Combining the TCS-PES approach with simulations confirms a downward band bending in the dark of -0.75 eV at the HTL|perovskite interface and an upward band bending of $+0.20$ eV at the perovskite|ETL interface.

An overall 0.80–0.90 eV difference can be deduced from the BE shifts of the Sn3d_{5/2} core level measured under dark and light. A 0.81 eV shift in electrostatic potential was already estimated at the HTL|perovskite interface. Therefore, it concludes that the main shift of electrostatic potential under illumination is present at the HTL|perovskite interface, also evidenced by the simulation (Figure 3b).

To obtain the value for the 0.8 V photovoltage with the 2D drift-diffusion simulations, we found that a small but relevant illumination needs to be present in the so-called dark condition.

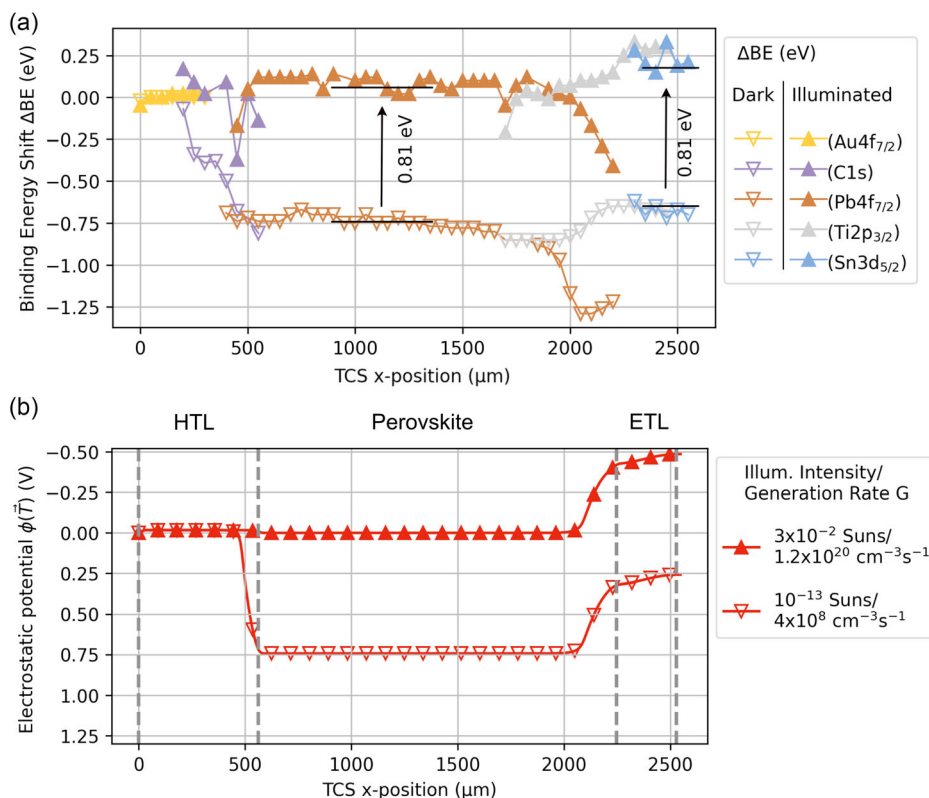


Figure 3. a) Experimental binding energy shifts ($BE_{\text{ref}} - BE$) as deduced from XPS line scans of Au4f_{7/2}, C1s, Pb4f_{7/2}, Ti2p_{3/2}, and Sn3d_{5/2} core levels. They respectively indicate the electrostatic potential over the contact layer (yellow), the HTL (purple), the perovskite layer (brown), and the ETL (gray and light blue). For each new layer, the overall BE difference was used as a starting point for the next layer. b) Electrostatic potential $\phi(\vec{r})$ under dark (10^{-13} sun) and under light (3×10^{-2} sun) from 2D drift-diffusion simulations.

Considering the material parameters as described in Table S1 (Supporting Information) and the generation rates corresponding to illumination intensities of 3×10^{-2} and 1×10^{-13} sun, respectively, the numerically derived electrostatic potentials along the tapered surface $\phi(\vec{T})$, match well with the experimentally measured BE shifts (Figure 3). Here, it is important to repeat that during the grinding process, TCS-PES preparation might not always yield a perfectly even surface. As a result, the lateral expansion of layers seen in TCS-PES might not perfectly correlate with the actual thickness of layers within a complete solar cell, as assumed for the simulations. This leads to a slight discrepancy with regard to the TCS x -position between simulation and experiment.

3.3. Extracting the Energetic Landscape of the Full Device

The good agreement between the PES measurement performed in only one direction (i.e., from the top Au contact to the bottom FTO contact) and the simulated data of the electrostatic potential on the tapered part $\phi(\vec{T})$ confirms the assumption that the 2D drift-diffusion simulation provides an accurate representation of the full device. Thus, the electrostatic potential in the full device $\phi(\vec{V})$ can be extracted from the numerical simulations and compared with the band structure of the taper part $\phi(\vec{T})$ for various simulated taper widths (Figure 4a). To compare the electrostatic potential at various locations, the normal position in the layer stack (as shown in Figure 2) is utilized as the common axis. We observe that the expected electrostatic potential at the complete part of the device $\phi(\vec{V})$ and the electrostatic potential along the TCS $\phi(\vec{T})$ are very similar.

The band structure in the dark and under illumination can be understood qualitatively as follows. In both the simulation and the experiment, under illumination, the band bending at the HTL|perovskite interface is strongly reduced while the band bending at the perovskite|ETL remains. This aligns well with the understanding that the HTL|perovskite interface is a p-n junction where the space charge region is reduced under illumination as the majority carrier quasi-Fermi levels are coupled to electrons in the perovskite and to holes in the HTL. Thus, the splitting of the quasi-Fermi levels under illumination leads to a reduction in the built-in field across the junction.

While there is also a built-in field at the perovskite|ETL interface due to a difference in Fermi levels, in our understanding this is an n-n-junction as the majority carrier quasi-Fermi levels are the same in this case. Thus, the splitting of the quasi-Fermi levels under illumination does not lead to a reduction in the built-in field across the junction. The fundamentals of this mechanism are discussed in Section S2 (Supporting Information). The full band structures including the respective quasi-Fermi levels can be extracted from the numerical simulations (Figure S6, Supporting Information) and they agree well with the approximated band structures from a previous publication.^[25] From an efficiency perspective, this decrease of the electrostatic potential at the perovskite|ETL interface forms a small energy barrier, reducing electron transfer and therefore solar cell performance.

3.4. Systematic Differences between $\phi(\vec{V})$ and $\phi(\vec{T})$

The strong similarity between $\phi(\vec{V})$ and $\phi(\vec{T})$ is striking and not intuitive. Therefore, we investigate, under which conditions this strong similarity between $\phi(\vec{V})$ and $\phi(\vec{T})$ persists and why differences emerge. To answer this question, we first focus on the influence of the geometry. 2D drift-diffusion simulations were performed for multiple structures with decreasing tapered widths under two different illumination conditions. As the tapered width approaches 0, meaning that the tapered cross-section becomes a vertical cross-section, $\phi(\vec{T})$ is expected to converge with $\phi(\vec{V})$. The electrostatic potentials $\phi(\vec{T})$ and $\phi(\vec{V})$ are depicted in Figure 4a. Changing the tapered width in the simulations from 6300 μm to 230 nm does not result in any significant change in the resulting electrostatic potential $\phi(\vec{T})$. The small differences are localized at the heterojunction interfaces. To quantify the differences to $\phi(\vec{V})$, we introduce

$$\phi_{RMS}(\vec{T}, \vec{V}) = \sqrt{\frac{\sum_y (\phi(\vec{T}(y)) - \phi(\vec{V}(y)))^2}{\sum_y 1}} \quad (6)$$

as a norm. As depicted in Figure 4b), for tapered widths larger than 18 μm , $\phi_{RMS}(\vec{T}, \vec{V})$ seems to stay constant, thus showing that above this value, a larger tapered width has a negligible

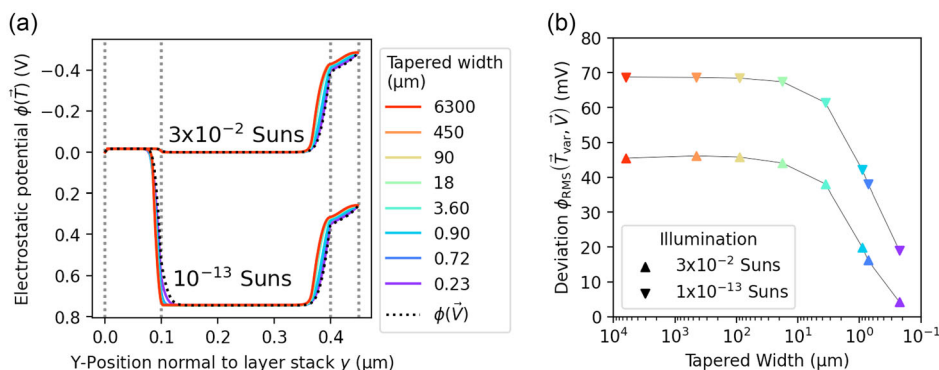


Figure 4. a) Electrostatic potential $\phi(\vec{T})$ and $\phi(\vec{V})$ of the simulated TCS of a PSC in the dark and under illumination for a tapered width ranging from 6.3 mm to 230 nm (i.e., a tapering angle of 0.0037° – 61°). b) RMS-Norm $\phi_{RMS}(\vec{T}, \vec{V})$, see Equation (7), between the electrostatic potential at various tapered widths $\phi(\vec{T})$ and electrostatic potential $\phi(\vec{V})$.

effect. Taking into account that typical PES setups have a spatial resolution of several hundreds of micrometers with the best coming close to 10 μm , and several spatially independent measurements are necessary to distinguish and investigate the different layers, it can be concluded that for the TCS-PES approach, the tapered width will always be larger than 18 μm .^[7] As the tapered width becomes small and the geometry converges with a “normal” cross-section, $\phi(\vec{T})$ also converges to $\phi(\vec{V})$, therefore, $\phi_{RMS}(\vec{T}, \vec{V})$ decreases as expected, see Figure 4b.

The change of the electrostatic potential is determined by space charge in the depletion/accumulation regions (i.e., space charge regions). Thus, comparing the 2D space charge region at the Spiro-OMeTAD|perovskite interface at a large (450 μm) and small (230 nm) tapered width gives insight into the behavior of $\phi(\vec{T})$ at different tapered widths. In the case of a small tapered width (Figure 5a), the space charge region encompasses a relatively large part of the perovskite layer that is not covered by the Spiro-OMeTAD, right of the red line. This lateral expansion is only in the order of 10 nm but is nevertheless significant due to the small overall tapered width of 230 nm (c.a., 5%). In the case of a large tapered width of 450 μm (Figure 5b), a lateral expansion in the order of 10 nm is indiscernible. This is also consistent with the TCS-PES measurement showing most of

the change in electrostatic potential of this interface in the Spiro-OMeTAD layer and no change of electrostatic potential in the perovskite (i.e., no binding energy shifts of $\text{Pb}4f_{7/2}$) (Figure 2a). Consequently, beyond a certain tapered width, any additional increase in the tapered width becomes insignificant, and the deviation $\phi_{RMS}(\vec{T}, \vec{V})$ remains constant which is consistent with Figure 4b.

With this lack of lateral influence at large tapered widths, the vertical segments of the TCS can be thought of as a series of independent planar (1D) layer stacks with decreasing layer thicknesses. PES measurements performed on the TCS at large tapered widths are thus equivalent to a classical step-by-step PES interface experiment for which PES measurements are alternated with stepwise deposition of material as well as PES depth profiling for which PES measurements are alternated with stepwise removal of material by Ar^+ or Ar -clusters sputtering (Figure 6a).^[8,17] This understanding has been confirmed by comparing electrostatic potentials at various vertical sections of the TCS with planar layer stacks having the same thickness, as depicted in Figure 6, and finding the differences to be negligible. Under the required tapered width for the TCS-PES approach, the TCS-PES results can always be interpreted similarly to classical PES interface experiments or depth profiling PES. It means that

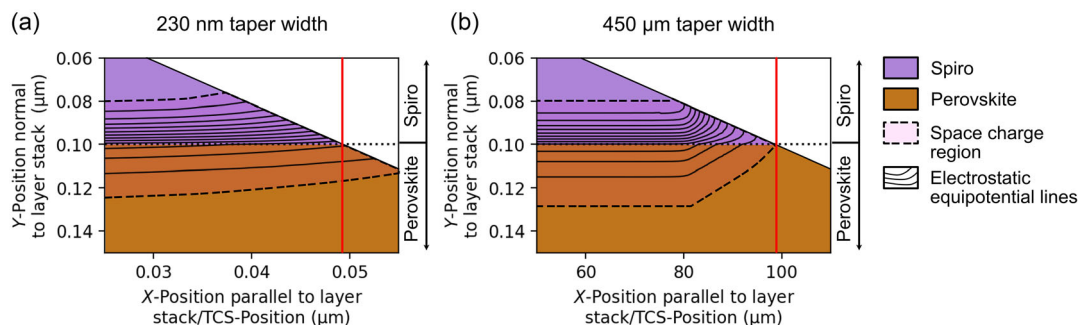


Figure 5. a) Space charge region shape at the perovskite|Spiro-OMeTAD interface for a simulated device with a small (230 nm) and b) a large (450 μm) tapered width. Note the different scaling of the x-axis between (a) and (b).

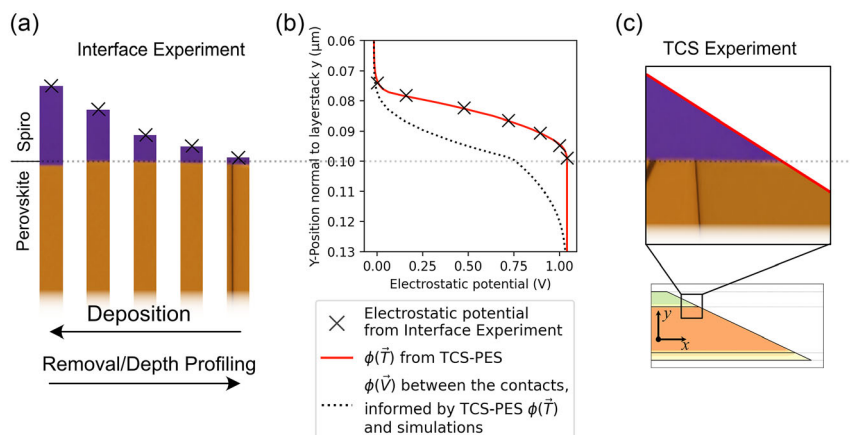


Figure 6. a) Schematic of a classical PES interface/depth profiling experiment. b) Simulated electrostatic potential in planar layer stacks (crosses) with different HTL thicknesses and electrostatic potential in a TCS with linearly increasing HTL thickness (red line) together with the reconstructed electrostatic potential c) Schematic of TCS-PES at the same interface.

all the existing literature for these approaches can be used to interpret the data obtained with the TCS-PES approach.

Nonetheless, the TCS-PES has numerous advantages in comparison to the more standard approaches. First, similarly to depth profiling it provides information on a complete device, there is no report yet of a full interface experiment from the bottom electrode to the top electrode. Second, it provides information about any kind of solar cell, independent of its fabrication process, and including state-of-the-art efficiency PSC produced from a liquid process, while interface experiments are limited to layers that can be only produced with vacuum deposition techniques.^[36–38] Finally, through the TCS the different interfaces are always accessible by moving the sample horizontally, for dark and light measurement, for instance, or for applying an external voltage, while interface and depth profiling PES experiments always require additional modifications of the sample between the PES measurements.

3.5. Under which Material Conditions are the Differences between $\phi(\vec{V})$ and $\phi(\vec{T})$ Small

While the geometry plays one role, the shape of space charge regions is also dependent on material parameters. To discuss generalized conditions for a good agreement between $\phi(\vec{T})$ and $\phi(\vec{V})$ from a material properties perspective, three distinct possibilities for space charge region widths within a PSC are considered in **Figure 7**. In case depicted in **Figure 7a**, the space charge regions at each heterojunction are small and most of the absorber is field-free. In the case of **Figure 7b**, the space charge regions extend over a significant part of the absorber, which correspondingly results in a net electric field across a significant part of the absorber. In case of **Figure 7c**, the space charge regions extend to widths where they would overlap. In this case, the net charge within each transport layer is not compensated within the absorber, but rather on the opposing transport layer. This leads to a so-called built-in field across the absorber.

Given the systematic error incurred in TCS-PES measurements at heterojunctions, the smaller the space charge region widths w , the better agreement between $\phi(\vec{V})$ and $\phi(\vec{T})$ can be expected. The general approximation of the space charge region (depletion) width w for an n-p-heterojunction,

$$w = \sqrt{\frac{2\epsilon_1\epsilon_2(N_A + N_D)^2}{q N_A N_D} \frac{V_{Bi}}{\epsilon_1 N_A + \epsilon_2 N_D}} \quad (7)$$

shows which material parameters are relevant: the space charge region becomes smaller with low permittivities ϵ of the respective materials, with a low offset between the respective Fermi levels V_{Bi} and/or with a higher amount of doping $N_A N_D$ (if the Fermi levels are already different, and the difference is not significantly increased by additional doping).

Given the layer thicknesses and assumptions of material properties (**Table S1**, Supporting Information), the junctions in the investigated device fulfill these conditions well. Perfect convergence between $\phi(\vec{T})$ and $\phi(\vec{V})$ is however not obtainable (see **Figure 5**), as the space charge regions around heterojunctions are always finite, thus 2D drift-diffusion simulations are needed for quantitative analysis.

For PSCs, a field-free absorber is a reasonable assumption due to the influence of mobile ions, even in the case of an undoped absorber (**Figure 7d**). While mobile ions were not explicitly considered within this work, from general understanding of their effect reported in the literature, they are expected to be distributed in a way that leads to the Fermi levels being mediated within very small regions at each absorber/transport layer interface, effectively forming very thin space charge regions.^[29,30,39–41] Therefore, $\phi(\vec{T})$ obtained with the TCS-PES approach on the perovskite solar cell discussed above, seems to be a reliable way to measure $\phi(\vec{V})$ and gather insights into the interface energetics of the device and its buried interfaces.

However, the TCS-PES approach could also be used to investigate any kind of solar cells that might not exhibit a predominantly field-free absorber, as depicted in **Figure 7c**. In that case, the interpretation becomes more challenging. If the charge regions are not mediated within the absorber, $\phi(\vec{T})$ and $\phi(\vec{V})$ differ and the $\phi(\vec{T})$ obtained with the TCS-PES approach misleads about the real electronic properties between the two contacts. We used different doping concentrations (undoped and doped with $4 \times 10^{17} \text{ cm}^{-3}$) to investigate the case of very small and very large space charge regions, respectively illustrated in **Figure 7a** and **7c**.

These electrostatic potential distributions $\phi(\vec{T})$ for the two different absorber doping concentrations and at various tapered widths are depicted in **Figure 8**. As discussed previously, in the doped case (**Figure 6a** and **7**), some unavoidable deviations are observed, and they increase as a function of the tapered width but remain close to $\phi(\vec{V})$. In contrast, for the undoped case (**Figure 7b**), $\phi(\vec{T})$ deviates from the targeted $\phi(\vec{V})$ and the TCS-PES approach does not give qualitative access to the buried interface energetics of a device, except with the help of 2D simulations.

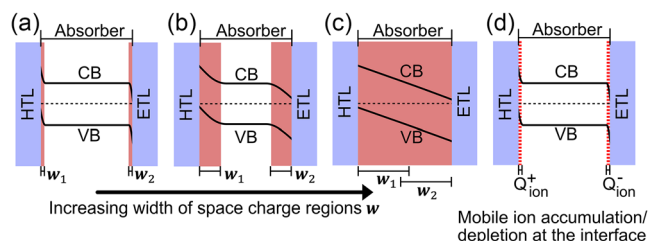


Figure 7. Schematic representation of band-bending in the absorber for varied space-charge region widths (in red) adjacent to the ETL/HTL. a) Narrow space charge regions at the heterojunctions leaving the bulk of the absorber field-free. b) Wider regions induce a net electric field in a substantial part of the absorber. c) Overlapping regions produce a field across the entire absorber. d) Mobile ions lead to ultra-thin space charge regions, keeping most of the absorber field-free.

4. Conclusion

The tapered cross-section photoelectron spectroscopy is a promising approach to investigate buried interfaces. Combining this experimental method with drift-diffusion 2D simulations is crucial to accurately determine the electrostatic potential of a

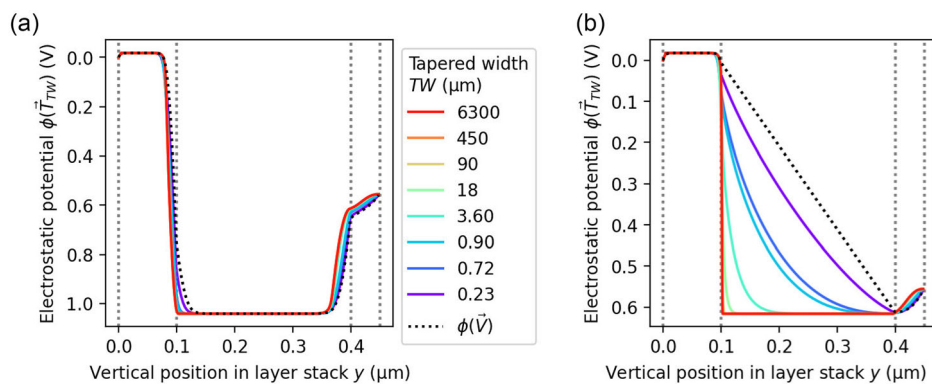


Figure 8. a) Electrostatic potential $\phi(\vec{r})$ for various tapered widths of the TCS-PSC with a doped absorber ($N_A = 4 \times 10^{17} \text{ cm}^{-3}$) and b) an undoped ($N_A = 0 \text{ cm}^{-3}$) absorber with no illumination.

complete solar cell from the measurements performed on the tapered part. We applied this approach to unravel the energetic landscape of perovskite solar cells.

The simulated electrostatic potential along the tapered cross-section reproduces the one measured by PES. It confirms the downward 0.75 eV band bending at the HTL|perovskite interface and an upward 0.2 eV band bending at the perovskite|ETL interface in the dark under open-circuit conditions. Under illumination, the first is flattened and the second remains due to the absence of photovoltage created at an n–n junction.

With a tapering angle low enough (i.e., below 2° which corresponds to a tapered width above $20 \mu\text{m}$) the electrostatic potential obtained with the TCS-PES approach is the same as the one from a standard step-by-step interface experiment. As the tapered width needs to be greater than $20 \mu\text{m}$ for discriminating the different layers of a standard PSC with the lateral resolution of a lab-based PES set-up, a TCS-PES can always be considered as a continuous interface experiment. Hence, all the existing knowledge obtained with this well-known approach for investigating buried interfaces can be transferred to the novel TCS-PES approach.^[42,43]

Finally, we explore the limitations of transferring the measurement results from a tapered cross-section to the electrostatic potential between the contacts in a generalized layer stack. The TCS-PES approach does not allow a straightforward interpretation of the buried interface energetics of a device without mostly field-free layers. Therefore, this process necessitates the support of 2D electrical simulations.

Supporting Information

Supporting Information is available from the Wiley Online Library or from the author.

Acknowledgements

The authors acknowledge funding from the Deutsche Forschungsgemeinschaft (DFG, German Research Foundation) within the SPP 2196 (grant no. INTERROGATE 423746744).

Open Access funding enabled and organized by Projekt DEAL.

Conflict of Interest

The authors declare no conflict of interest.

Data Availability Statement

The data that support the findings of this study are available from the corresponding author upon reasonable request.

Keywords

energetic landscape, perovskite solar cells, photoelectron spectroscopy, tapered cross section, 2D drift-diffusion simulations

Received: May 11, 2023
Revised: July 26, 2023
Published online: August 20, 2023

- [1] J. Park, J. Kim, H.-S. Yun, M. J. Paik, E. Noh, H. J. Mun, M. G. Kim, T. J. Shin, S. I. Seok, *Nature* **2023**, 616, 724.
- [2] L. Schmidt-Mende, V. Dyakonov, S. Olthof, F. Ünlü, K. M. T. Lê, S. Mathur, A. D. Karabanov, D. C. Lupascu, L. M. Herz, A. Hinderhofer, F. Schreiber, A. Chernikov, D. A. Egger, O. Shargaieva, C. Cocchi, E. Unger, M. Saliba, M. M. Byrnavand, M. Kroll, F. Nehm, K. Leo, A. Redinger, J. Höcker, T. Kirchartz, J. Warby, E. Gutierrez-Partida, D. Neher, M. Stollerfoht, U. Würfel, M. Unmüßig, et al., *APL Mater.* **2021**, 9, 109202.
- [3] P. Schulz, D. Cahen, A. Kahn, *Chem. Rev.* **2019**, 119, 3349.
- [4] S. Béchu, M. Ralaivisoa, A. Etcheberry, P. Schulz, *Adv. Energy Mater.* **2020**, 10, 1904007.
- [5] S. Tao, I. Schmidt, G. Brocks, J. Jiang, I. Tranca, K. Meerholz, S. Olthof, *Nat. Commun.* **2019**, 10, 2560.
- [6] C. Maheu, M. A. Z. Pour, I. Damestoy, D. Ostheimer, M. Mellin, D. C. Moritz, A. Paszuk, W. Jaegermann, T. Mayer, T. Hannappel, J. P. Hofmann, *Adv. Mater. Interfaces* **2023**, 10, 2201648.
- [7] W. E. S. Unger, J. M. Stockmann, M. Senoner, T. Weimann, S. Bütefisch, C. Passiu, N. D. Spencer, A. Rossi, *J. Vac. Sci. Technol. A* **2020**, 38, 053206.
- [8] A. Klein, T. Mayer, A. Thissen, W. Jaegermann, in *Methods in Physical Chemistry*, John Wiley & Sons, Ltd., Hoboken, NJ **2012**, pp. 477–512.
- [9] F. Zu, M. Roß, L. Frohloff, D. Shin, N. Tessler, S. Albrecht, N. Koch, *Sol. RRL* **2022**, 6, 2101065.

- [10] F. Zu, J. H. Warby, M. Stolterfoht, J. Li, D. Shin, E. Unger, N. Koch, *Phys. Rev. Lett.* **2021**, 127, 246401.
- [11] S. Chen, T. W. Goh, D. Sabba, J. Chua, N. Mathews, C. H. A. Huan, T. C. Sum, *APL Mater.* **2014**, 2, 081512.
- [12] C. Wang, X. Liu, C. Wang, Z. Xiao, C. Bi, Y. Shao, J. Huang, Y. Gao, *J. Vac. Sci. Technol. B* **2015**, 33, 032401.
- [13] G. Ji, G. Zheng, B. Zhao, F. Song, X. Zhang, K. Shen, Y. Yang, Y. Xiong, X. Gao, L. Cao, D.-C. Qi, *Phys. Chem. Chem. Phys.* **2017**, 19, 6546.
- [14] P. Schulz, E. Edri, S. Kirmayer, G. Hodes, D. Cahen, A. Kahn, *Energy Environ. Sci.* **2014**, 7, 1377.
- [15] T. Hellmann, C. Das, T. Abzieher, J. A. Schwenzler, M. Wussler, R. Dachauer, U. W. Paetzold, W. Jaegermann, T. Mayer, *Adv. Mater.* **2020**, 10, 2002129.
- [16] T. Hellmann, M. Wussler, C. Das, R. Dachauer, I. El-Helaly, C. Mortan, T. Mayer, W. Jaegermann, *J. Mater. Chem. C* **2019**, 7, 5324.
- [17] C. Noël, S. Pescetelli, A. Agresti, A. Franquet, V. Spampinato, A. Felten, A. di Carlo, L. Houssiau, Y. Busby, *Materials* **2019**, 12, 726.
- [18] S. Cacovich, P. Dally, G. Vidon, M. Legrand, S. Gbegnon, J. Rousset, J.-B. Puel, J.-F. Guillemoles, P. Schulz, M. Bouttemy, A. Etcheberry, *ACS Appl. Mater. Interfaces.* **2022**, 14, 34228.
- [19] Y. J. Hofstetter, Y. Vaynzof, *ACS Appl. Polym. Mater.* **2019**, 1, 1372.
- [20] C. Das, W. Zia, C. Mortan, N. Hussain, M. Saliba, J. Ingo Flege, M. Kot, *Sol. RRL* **2021**, 5, 2100298.
- [21] M. Wussler, T. Mayer, C. Das, E. Mankel, T. Hellmann, C. Prabowo, I. Zimmermann, M. K. Nazeeruddin, W. Jaegermann, *Adv. Funct. Mater.* **2020**, 30, 1910679.
- [22] B. Philippe, M. Saliba, J.-P. Correa-Baena, U. B. Cappel, S.-H. Turren-Cruz, M. Grätzel, A. Hagfeldt, H. Rensmo, *Chem. Mater.* **2017**, 29, 3589.
- [23] T. Greunz, B. Strauß, S. E. Schausberger, B. Heise, B. Jachs, D. Stifter, *Anal. Bioanal. Chem.* **2013**, 405, 7153.
- [24] G. Säckl, J. Duchoslav, R. Pugstaller, C. Marchfelder, K. Haselgrübler, M. Aufray, D. Stifter, G. M. Wallner, *Polymers* **2022**, 14, 2226.
- [25] C. Das, M. Wussler, T. Hellmann, T. Mayer, I. Zimmermann, C. Maheu, M. K. Nazeeruddin, W. Jaegermann, *ACS Appl. Mater. Interfaces* **2020**, 12, 40949.
- [26] Synopsys]EDA Tools, Semiconductor IP and Application Security Solutions, <https://www.synopsys.com/> (accessed: July 2023).
- [27] S. Li, Y.-L. Cao, W.-H. Li, Z.-S. Bo, *Rare Met.* **2021**, 40, 2712.
- [28] C.-C. Chueh, C.-Z. Li, A. K.-Y. Jen, *Energy Environ. Sci.* **2015**, 8, 1160.
- [29] J. Thiesbrummel, V. M. Le Corre, F. Peña-Camargo, L. Perdigón-Toro, F. Lang, F. Yang, M. Grischek, E. Gutierrez-Partida, J. Warby, M. D. Farrar, S. Mahesh, P. Caprioglio, S. Albrecht, D. Neher, H. J. Snaith, M. Stolterfoht, *Adv. Mater.* **2021**, 11, 2101447.
- [30] J. Herterich, C. Baretzky, M. Unmüßig, C. Maheu, N. Glissmann, J. Gutekunst, G. Loukeris, T. Mayer, M. Kohlstädt, J. P. Hofmann, U. Würfel, *Sol. RRL* **2022**, 6, 2200195.
- [31] L. M. Herz, *ACS Energy Lett.* **2017**, 2, 1539.
- [32] T. Kirchartz, J. A. Márquez, M. Stolterfoht, T. Unold, *Adv. Energy Mater.* **2020**, 10, 1904134.
- [33] L. Yang, J. Feng, Z. Liu, Y. Duan, S. Zhan, S. Yang, K. He, Y. Li, Y. Zhou, N. Yuan, J. Ding, S. Liu (Frank), *Adv. Mater.* **2022**, 34, 2201681.
- [34] J. Wang, F. Meng, R. Li, S. Chen, X. Huang, J. Xu, X. Lin, R. Chen, H. Wu, H.-L. Wang, *Sol. RRL* **2020**, 4, 2000091.
- [35] M. Kot, L. Kegelmann, H. Köbler, M. Vorokhta, C. Escudero, P. Kúš, B. Šmíd, M. Tallarida, S. Albrecht, A. Abate, I. Matolínová, D. Schmeißer, J. I. Flege, *ChemSusChem* **2020**, 13, 5722.
- [36] L. Gil-Escrig, C. Momblona, M.-G. La-Placa, P. P. Boix, M. Sessolo, H. J. Bolink, *Adv. Mater.* **2018**, 8, 1703506.
- [37] J. Li, H. Wang, X. Y. Chin, H. A. Dewi, K. Vergeer, T. W. Goh, J. W. M. Lim, J. H. Lew, K. P. Loh, C. Soci, T. C. Sum, H. J. Bolink, N. Mathews, S. Mhaisalkar, A. Bruno, *Joule* **2020**, 4, 1035.
- [38] Y.-H. Chiang, M. Anaya, S. D. Stranks, *ACS Energy Lett.* **2020**, 5, 2498.
- [39] L. Bertoluzzi, C. C. Boyd, N. Rolston, J. Xu, R. Prasanna, B. C. O'Regan, M. D. McGehee, *Joule* **2020**, 4, 109.
- [40] S. A. L. Weber, I. M. Hermes, S.-H. Turren-Cruz, C. Gort, V. W. Bergmann, L. Gilson, A. Hagfeldt, M. Graetzel, W. Tress, R. Berger, *Energy Environ. Sci.* **2018**, 11, 2404.
- [41] V. M. Le Corre, J. Diekmann, F. Peña-Camargo, J. Thiesbrummel, N. Tokmoldin, E. Gutierrez-Partida, K. P. Peters, L. Perdigón-Toro, M. H. Futscher, F. Lang, J. Warby, H. J. Snaith, D. Neher, M. Stolterfoht, *Sol. RRL* **2022**, 6, 2100772.
- [42] E. Mankel, C. Hein, M. Kühn, T. Mayer, *Phys. Status Solidi A* **2014**, 211, 2040.
- [43] M. Frericks, C. Pflumm, E. Mankel, T. Mayer, W. Jaegermann, *ACS Appl. Electron. Mater.* **2021**, 3, 1211.